Analyst

Quantitative analysis of biochemical processes in living cells at a single-molecule level: a case of olaparib-PARP1 (DNA repair protein) interactions

Journal:	*Analyst*
Manuscript ID	AN-ART-09-2021-001769.R1
Article Type:	Paper
Date Submitted by the Author:	18-Oct-2021
Complete List of Authors:	Karpinska, Aneta; Institute of Physical Chemistry Polish Academy of Sciences, Department of Soft Condensed Matter Pilz, Marta; Institute of Physical Chemistry Polish Academy of Sciences, Department of Soft Condensed Matter Buczkowska, Joanna; Institute of Physical Chemistry Polish Academy of Sciences, Department of Soft Condensed Matter Żuk, Paweł; Institute of Physical Chemistry Polish Academy of Sciences, Department of Soft Condensed Matter; Lancaster University, Department of Physics Kucharska, Karolina; Institute of Physical Chemistry Polish Academy of Sciences, Department of Soft Condensed Matter Magiera, Gaweł; Poznan University of Medical Sciences, Department of Medicine Kwapiszewska, Karina; Institute of Physical Chemistry Polish Academy of Sciences, Holyst, Robert; Institute of Physical Chemistry Polish Academy of Sciences, Department of Soft Condensed Matter

ARTICLE Journal Name

Quantitative analysis of biochemical processes in living cells at a single-molecule level: a case of olaparib-PARP1 (DNA repair protein) interactions

Received 00th January 20xx,
Accepted 00th January 20xx

DOI: 10.1039/x0xx00000x

Aneta Karpińska[a], Marta Pilz[a], Joanna Buczkowska[a], Paweł J. Żuk[ab], Karolina Kucharska[a], Gaweł Magiera[c], Karina Kwapiszewska[a]* and Robert Hołyst[a]*

Quantitative description of biochemical processes inside living cells and at single-molecule levels remains a challenge at the forefront of modern instrumentation and spectroscopy. This paper demonstrates such single-cell, single-molecule analyses performed to study the mechanism of action of olaparib – an up-to-date, FDA-approved drug for germline-BRCA mutated metastatic breast cancer. We characterized complexes formed with PARPi-FL - fluorescent analog of olaparib *in vitro* and in cancer cells using the advanced fluorescent-based method: Fluorescence Correlation Spectroscopy (FCS) combined with a length-scale dependent cytoplasmic/nucleoplasmic viscosity model. We determined *in vitro* olaparib – PARP1 equilibrium constant ($6.06 \cdot 10^8$ mol/L^{-1}). In the cell nucleus, we distinguished three states of olaparib: freely diffusing drug (24%), olaparib – PARP1 complex (50%), and olaparib – PARP1 – RNA complex (26%). We show olaparib accumulation in 3D spheroids, where intracellular concentration is twofold higher than in 2D cells. Moreover, olaparib concentration was tenfold higher (506 nmol/L vs. 57 nmol/L) in cervical cancer (BRCA1 high abundance) than in breast cancer cells (BRCA1 low abundance) but with a lower toxic effect. Thus we confirmed that the amount of BRCA1 protein in the cells is a better predictor of the therapeutic effect of olaparib than its penetration into cancer tissue. Our single-molecule and single-cell approach give a new perspective of drug action in living cells. FCS provides a detailed *in vivo* insight, valuable in drug development and targeting.

Introduction

Several biochemical processes occur after drug penetration into the cell, involving interactions with various cellular structures, proteins, and genetic material. Therefore, the therapeutic drug effect depends on several interrelated processes taking place in living cells. Detection of intracellular interactions at a quantitative level may allow for the more specific design of subsequent drug candidates. Most of the methods used and developed to study such interactions are qualitative or semi–qualitative (flow cytometry, confocal imaging). There are purely quantitative techniques, such as *ex vivo* biochemical assays or Förster Resonance Energy Transfer (FRET)[1], used to quantify intracellular interactions. However, most existing quantitative methods have several limitations in their application in living cells, such as sample fixation[2] or, as in the FRET method, the need to inject labeled protein.

As an alternative, to provide quantitative data from the cellular interior, we used Fluorescence Correlation Spectroscopy (FCS) coupled with detailed biophysical models for measurements directly in living cells. FCS is a non-invasive method that allows the measurement of probes at physiological concentrations (on the order of nmol/L). Its application to cells does not need prior fixation and requires only one fluorescent species, so measurements are performed on cells with metabolism unchanged by external factors. The FCS provides information about diffusion coefficient, probe size, concentration, or intracellular interactions. The probe size or interactions are obtained based on a length-scale dependent cytoplasmic/nucleoplasmic viscosity model we previously described[3–5]. Our powerful model has been validated in various biological systems, including cancer and normal cells, both mesenchymal or epithelial.

The present study provides for the first time quantitative data on the uptake and intracellular interactions of the fluorescent derivative of olaparib (PARPi-FL) in triple-negative breast cancer (TNBC) cells. The principle of action of olaparib is to prevent the repair of damaged DNA (Fig. 1). Genetic material constantly undergoes damage, approximately at a rate of 10,000 to 1,000,000 molecular defects per cell per day[6]. The accumulation of abnormalities in DNA leads to permanent genetic mutations, as well as cell death, which is desirable for cancer cells. However, DNA damages are eliminated by specialized repair systems, such as base excision repair (BER) or non-homologous end joining (NHEJ). In DNA break repair, the PARP1 protein is involved. It is the first line of response to the resulting damage to genetic material, facilitating the selection of the repair process pathway[7]. PARP1 binds to a DNA strand by a domain located at the N-terminus of the polypeptide chain. DNA break repair by the PARP1 protein relies on the process of autoPARylation. The formed poly (ADP-ribose) (PAR) polymers bind to breaks formed in DNA. Due to the negative charge of PAR polymers[8], the PARP1 protein dissociates from the DNA strand, recruiting repair enzymes.

[a] *Institute of Physical Chemistry Polish Academy of Sciences, Kasprzaka 44/52, 01-224 Warsaw, Poland*
[b] *Department of Physics, Lancaster University, Lancaster LA1 4YB, United Kingdom*
[c] *Department of Medicine, Poznan University of Medical Sciences, 60-356, Poznan, Poland*
* E-mail: rholyst@ichf.edu.pl; kkwapiszewska@ichf.edu.pl
Electronic Supplementary Information (ESI) available. See DOI: 10.1039/x0xx00000x

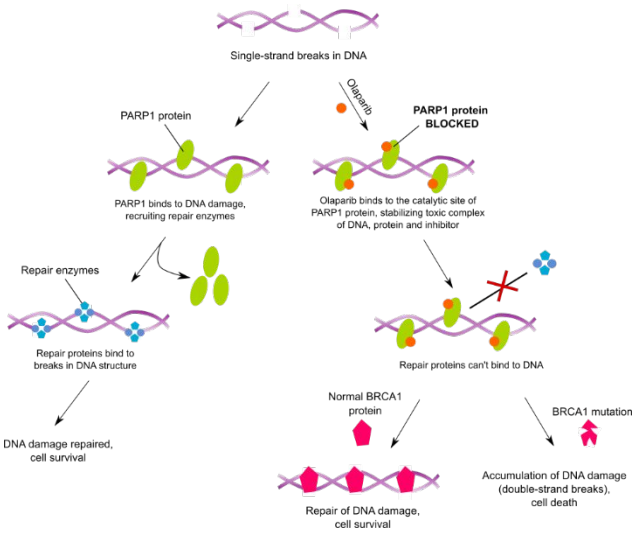

Fig. 1 The principle of action of olaparib. The PARP1 protein binds to DNA strand breaks and recruits repair enzymes by dissociating itself. In the presence of olaparib, which interacts with the catalytic domain of the protein, PARP1 protein is blocked, leading to stabilization of olaparib – PARP1 – DNA complexes. The accumulation of single DNA strand breaks leads to double-strand breaks, which can be repaired by BRCA1 protein. As a result, the cell survives. However, if BRCA1 protein is mutated, the DNA damage cannot be efficiently repaired, and the cell dies, which is desirable for cancer cell treatment.

Nevertheless, there are molecules like olaparib that, by competing with NAD^+ for a binding site in the PARP1 catalytic domain, inhibit PAR formation[9]. It results in the entrapment of PARP1 at the site of DNA damage and thus blocks access to the damage for repair proteins. The accumulation of single-strand DNA breaks leads to double-strand breaks. Two pathways are then possible, depending on whether the cell has BRCA1 mutation or not. If the BRCA1 protein is at a normal level, the DNA double breaks are repaired by homologous recombination, and the cell survives. The process is different for cells with the BRCA1 mutation. In this case, the DNA damage is not efficiently repaired, resulting in the activation of signaling pathways that lead to cell death.

Results shown in this paper contribute to a better understanding of the tested drug's mechanisms, precisely characterizing the different components present inside cells and interacting with the olaparib analog. We identified three mobile components in the nucleus of MDA-MB-231 cells: a) freely diffusing tested drug, b) complex of olaparib analog and PARP1 protein c) interactions with long RNA (most probably mRNA or long-non-coding RNA). Using the *in vitro* equilibrium constant, we determined the precise total concentration of PARP1 protein not bound to DNA. The study was also extended to the cytoplasm. There, we also identified the freely diffusing PARP1 bound in complex with the tested drug. All the results obtained in TNBC cells were compared with Cervical Cancer (CC) cells (HeLa cell line). Based on proteomic data, we can conclude that the higher accumulation of olaparib derivative in CC cells is related to the expression level of PARP1 protein. However, the drug's therapeutic effect is not positively dependent on the amount of PARP1 in the cell. Most probably, olaparib therapy's effectiveness depends on the expression level of BRCA1 protein, which is involved in DNA repair. The more BRCA1, the better the cell counteracts the effects caused by the drug.

Experimental

Reagents

The olaparib derivative named PARPi-FL with catalog number 6461 used in this study was ordered from Tocris Bioscience (Bristol, UK). A stock solution was prepared according to the manufacturer's protocol. 1 mg of the compound was dissolved in 1.56 ml of sterile dimethyl sulfoxide (DMSO, Sigma-Aldrich) to a concentration of 1 mmol/L and stored at -20˚C.

The PARP1 protein used to determine the hydrodynamic radius of the protein-inhibitor complex and to define the equilibrium constant in a buffer was purchased from Thermo Fischer Scientific (Waltham, Massachusetts, USA). The name of this product is Human PARP1, His Tag Recombinant Protein, catalog number: # A42574. The protein was dissolved in a buffer containing 50 mmol/L 2-Amino-2-(hydroxymethyl)propane-1,3-diol (TRIS, Carl Roth), 100 mmol/L sodium chloride (NaCl, Avantor), and 10% glycerol (Sigma-Aldrich). The stock solution thus obtained was then diluted to working concentration in sterile Phosphate-Buffered Saline (PBS, Sigma-Aldrich) and stored at -20˚C.

The ability of PARP1 protein to bind with RNA molecules was determined using the product from Thermo Fischer Scientific (Waltham, Massachusetts, USA) called RNA control 250, catalog number: # AM7155. The solution was stored at -20˚C.

Cell Culture

MDA-MB-231 and HeLa cells came from the American Type Culture Collection (ATCC, Manassas, USA). Both cell lines were cultured as a standard monolayer in the complete growth medium, supplemented with fetal bovine serum (FBS, Gibco), L-glutamine 1% v/v (Sigma-Aldrich), and the antibiotics: streptomycin [10 000 U/ml] and penicillin [10 mg/ml] 1% v/v (Sigma-Aldrich). Cultures were performed under standard conditions (37˚C, 5% CO_2). HeLa cell lines were cultured in Dulbecco's Modified Eagle Medium (DMEM) with low glucose content (Institute of Immunology and Experimental Technology, Wrocław, Poland), while the basal medium for MDA-MB-231 was RPMI 1640 with sodium bicarbonate and without L-glutamine (Sigma-Aldrich). Using regular passages, cells were maintained in a logarithmic growth phase. To detach cells from the surface, 0.25% Trypsin-EDTA solution (Sigma-Aldrich) was used. The trypsinization process was controlled by light microscopy.

For FCS measurements or confocal imaging, cells were grown on an 8-chamber cover glass Ibidi® (Germany) slide. After 24h of cell incubation (approx. 60% of confluence), FCS and confocal experiments were performed. Multicellular spheroids were obtained by culturing cells on a non-adhesive surface - Nunclon™ Sphera™ dish (ThermoFisher Scientific). Cultures were performed in an incubator providing an optimal temperature - 37˚C and a 5% CO_2 concentration. A complete culture medium without phenol red, suitable for MDA-MB 231

or HeLa (Sigma-Aldrich), was used. On the fifth day, the culture suspension was transferred to the measuring plate - an 8-chambered glass coverslip (CellVis) - on which spheroids were deposited, and all experiments were performed. The preparation of 3D culture compatible with FCS measurements was previously described[10].

MTT assay

Experiments proceeded with cell number optimization. This step was performed according to the ATCC protocol (*MTT Cell Proliferation Assay ATCC, 2011*).

The initial cell solution was diluted to approximately number – 1 000 cells/well for MDA-MB-231 and 5 000 cells/well for HeLa (controlled with Countess II Cell Counter) and seeded into a 96-well plate (Greiner Bio-One). Then, cells were incubated 24h at 37˚C to enable cell attachment. The medium was removed, and PARPi-FL at the different concentrations (0.625 –160 µmol/L for MDA-MB-231, 0.156 – 80 µmol/L for HeLa) was added to the cell fresh medium. Three repeats were performed for each concentration. Controls were also performed three times: blank - medium without cells, positive control - cells not treated with PARPi-FL and negative control - dead cells, toxicant - 1% Triton-X 100 (Sigma-Aldrich).

The plate was incubated at 37°C for 72 hours. After this time, the medium was replaced with a culture medium including 1 mmol/L 3-(4,5-dimethylthiazol-2-yl)-2,5-diphenyltetrazolium bromide (MTT reagent, Thermo Fischer Scientific). Negative controls additionally contained 1% Triton-X 100. Cells were incubated for 4 hours at 37 °C. The solutions were replaced with DMSO and incubated for 10 minutes. The absorbance in each well was measured at 540 nm using a Synergy HTX multi-mode reader (BioTek).

AlamarBlue® assay

The dye was applied according to the manufacturer's protocol (*General Method for Measuring Cytotoxicity or Proliferation Using alamarBlue® by Fluorescence, Bio-Rad*). Five controls were performed per assay: a) medium alone with dye (blank), b) cells with alamarBlue® untreated with PARPi-FL (positive control), c) dead cells with alamarBlue®, toxicant - 1% Triton-X 100 (negative control), d) a pure medium without dye and e) cells untreated with the tested compound without alamarBlue® (autofluorescence control). After 72h of cell incubation at 37˚C, 10% alamarBlue® dye was added in phenol red-free culture medium (to eliminate the background fluorescence of phenol red). Incubation with the dye at 37 °C lasted for 4 hours. After this time, the fluorescence in each well was measured at 590 nm (590/20 filter) for excitation at 560 nm (560/20 filter).

Plots of cell viability were made by taking averages of the three repeats and using a logarithmic scale on the x-axis. A logistic dose-response function including four parameters, derived from the Origin2019b program, was fitted to the measurement points.

FCS setup

FCS measurements were performed using a Nikon Eclipse TE2000U confocal microscope coupled to a Pico Harp 300 FCS equipment (PicoQuant, Germany). Observations were performed using a 60x objective (N.A. 1.2) with water immersion. A 485 ± 3 nm pulsed diode laser was used to excite PARPi-FL fluorescence. The fluorescence photons were collected by Single-Photon Avalanche Diodes (MPD and PerkinElmer), through a 488 long-pass filter (Chroma, USA) positioned in the optical path in front of the detector.

A calibration procedure preceded each measurement. During calibration, we characterized the confocal volume using a nanomolar solution of rhodamine 110 with a well-known diffusion coefficient. We maintained a similar refractive index of calibration solution as a studied system by using two different solutions: rhodamine 110 in PBS for *in vitro* measurements and rhodamine 110 in 2.5% glucose in PBS for measurements inside cells[11].

The set temperature (36 ± 0.5˚C) was maintained by a climate chamber (Okolab, Italy). In the intracellular FCS measurements, the detection volume was positioned in the cytosol/nucleus using the imaging mode of the microscope. The accuracy of alignment was within 0.5 µm. Once the detection position determined, we switched to the FCS mode, and the data were acquired.

FCS data were fitted using Equation 1.

$$G(\tau) = \frac{1}{N}\left(1 + \frac{\theta_{trip}}{1-\theta_{trip}}\exp\left(-\frac{\tau}{\tau_{trip}}\right)\right)\sum_{i=1}^{n} A_i \frac{1}{1+\left(\frac{\tau}{\tau_{Di}}\right)}\frac{1}{\sqrt{1+\frac{1}{\kappa^2}\left(\frac{\tau}{\tau_{Di}}\right)}} \quad (1)$$

where N corresponds to overall particle number in confocal volume, $\boldsymbol{\theta_{trip}}$ – a fraction of particles in a triplet state, $\boldsymbol{\tau_{Di}}$ stands for the diffusion time of the i-th diffusing component, A_i is the amplitude of the i-th component while $\boldsymbol{\kappa}$ corresponds to the aspect ratio of the Gaussian used to approximate the focus. The parameter $\boldsymbol{\kappa}$ was determined during calibration and was kept in the range of 5.5-6.5.

Fitting the appropriate mathematical model to the obtained FCS curves was carried out using the QuickFit 3.0 software (DKFZ, Germany). The parameter to be fitted is the diffusion time of the component(s) (depending on the mathematical model applied). Based on the value of τ_D, the diffusion coefficient given by Equation 2 is determined.

$$\boldsymbol{D} = \frac{\boldsymbol{\omega_{xy}}^2}{\boldsymbol{4\tau_D}} \quad (2)$$

where $\boldsymbol{\omega_{xy}}$ corresponds to the dimension of a focal volume defined during calibration.

FCS measurements in a buffer (*in vitro*)

The hydrodynamic radius of the PARPi-FL molecule and the PARP1 – PARPi-FL complex was determined in PBS solution at 36˚C using an FCS setup. The concentration of the PARPi-FL compound in both cases was 10 nmol/L. PARP1 protein was used at a concentration of 10 nmol/L, the same as RNA molecule. Each time, ten independent measurements lasting 60

s were performed. The hydrodynamic radius, R_h was calculated using the Stokes-Sutherland-Einstein equation:

$$R_h = \frac{k \cdot T}{6 \cdot \pi \cdot \eta \cdot D} \quad (3)$$

where k is Boltzmann's constant, T stands for the absolute temperature, η corresponds to the solvent viscosity.

FCS measurements directly in living cells (*in vivo*)

The principle of performing FCS measurements directly in living cells is shown in Fig. 2. In the first step, the confocal volume was positioned in the cell compartment of interest (the nucleus or cytoplasm), approximately 2 µm above the glass. The FCS measurements within spheroids were performed at a maximum depth of 35 µm from the glass. The SymphoTime software (PicoQuant, Germany) then captured a fluctuation record of the fluorescence intensity of molecules diffusing through this volume. By using mathematical processing, the fluctuations were represented as an autocorrelation curve. An appropriate mathematical model (one, two, or three-component 3D normal diffusion), describing the process occurring in the tested area of the cell, was then fitted to the FCS curve.

For both 2D and 3D cell measurements, 10 cells were measured each time, taking 3-8 individual measurements per cell.

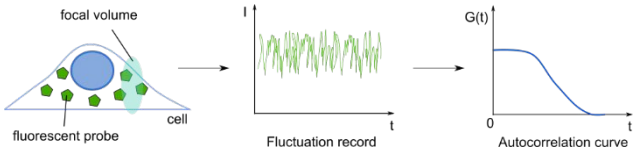

Fig. 2 Scheme of the FCS experiment directly in living cells.

Cytoplasm nanoviscosity of MDA-MB-231

TRITC-labeled dextrans (Sigma-Aldrich) and nanospheres (Siliquan, Poland) were introduced into the cytoplasm of MDA-MB-231 cells by using Cell-IN product (Poland). Calcein-AM (Sigma-Aldrich) was spontaneously uptaken by cells. EGFP was expressed after transfection with appropriate plasmids. FCS measurements were performed as described above. Detailed protocols were previously reported[3,5].

Determination of partition coefficient

The partition coefficient was determined as the ratio of the concentration inside the cell to the concentration in the culture medium. 3-4 independent concentrations were examined. Concentrations in the medium were determined by positioning the confocal focus outside the cell, in the medium surrounding the cell. Before measurements, cells were not washed to prevent drug outflow.

Confocal imaging

We used confocal microscopy to visualize the penetration of PARPi-FL into two- and three-dimensional cell cultures. The fluorescence signal of the olaparib analog comes from the BODIPY-FL dye attached to the molecule, which emits radiation at a wavelength λ_{max}= 513 nm when excited with a 485 nm laser. The equipment included a Nikon A1 confocal microscope with a climate chamber (Laboratory of microfabrication, IPC PAS, Poland).

3D imaging was started immediately after adding PARPi-FL to the medium with spheroids to a final concentration of 60 nmol/L. The imaging procedure took about 25 min. After this time, without changing any of the settings, another scan was done to observe potential differences in signal intensity depending on the time of incubation of the spheroids with the drug. We used a spectral detector, which allows separation of the recorded radiation with a resolution of up to 2.5 nm, to eliminate the autofluorescence signal.

Brightness method

The equilibrium constant of the PARP1 – inhibitor complex in a buffer (*in vitro*) was determined by using the previously described brightness method[12,13], based on a change of molecular brightness (MB) upon the reaction. The inhibitor molecule bound to the protein emits a smaller number of photons compared to a sample containing the freely diffusing inhibitor.

Molecular brightness is defined as:

$$MB = \frac{I}{N_{molecules}} \quad (4)$$

where I is intensity of fluorescence, measures as number of detected photons, $N_{molecules}$ is number of molecules present in confocal volume.

Equation 5 was used to determine the fluorescence intensity of the free inhibitor.

$$I_1 = V_o \cdot N_A \cdot C_{Parpi-FL} \cdot \alpha \quad (5)$$

where V_0 [dm^3] corresponds to a focal volume defined during calibration, N_A – the Avogadro number, $C_{PARPi\text{-}FL}$ [mol/L] is the concentration of the inhibitor equal to 10 nmol/L and α stands for a MB of the freely diffusing PARPi-FL.

For the reaction of the PARPi-FL with PARP1, Equation 6 can be written.

$$PARP1 + PARPi-FL \overset{K}{\leftrightarrow} PARP1-PARPi-FL \quad (6)$$

The expression for the equilibrium constant is given by the formula:

$$K = \frac{C^{eq}_{PARP1-PARPi-FL}}{C^{eq}_{PARP1} \cdot C^{eq}_{PARPi-FL}} = \frac{C^{eq}_{PARP1-PARPi-FL}}{(C_{PARP1} - C^{eq}_{PARP1-PARPi-FL}) \cdot (C_{PARPi-FL} - C^{eq}_{PARP} \quad (7)$$

The Equation 7 can be solved as:

$$C^{eq}_{PARP1-PARPi-FL} = \frac{1}{2}\cdot \left(C_{PARP1} + C_{PARPi-FL} + \frac{1}{K} - \sqrt{\left(-C_{PARP1} - C_{PARPi-FL} - \frac{1}{K}\right)^2 - 4\cdot C_{PARP1}\cdot C_{PARPi-FL}}\right) \quad (8)$$

The formed protein – inhibitor complex had a lower fluorescence intensity than the MB of the free inhibitor. The molecular brightness of the complex was determined as γ.

The expression for the fluorescence intensity of the complex formed is presented in Equation 9.

$$I_2 = V_o \cdot N_A \cdot \left(\alpha \cdot C^{eq}_{PARPi-FL} + \gamma \cdot C^{eq}_{PARPi-FL-PARP1}\right) \quad (9)$$

When the complex is formed, the recorded fluorescence comes from two molecules: the complex and freely diffusing PARPi-FL. By determining the fluorescence intensity for different concentrations of PARP1 protein at a given (= 10 nmol/L) concentration of free inhibitor, a curve of the dependence of the number of photons on the protein concentration was obtained. The higher the protein concentration, the lower the intensity value. Experimental points were fitted using the following equation, resulting from the transformation of Equation 9 based on the expression for the equilibrium constant.

$$I_2 = V_o \cdot N_A \cdot \alpha \cdot \left[C_{PARPi-FL} - C^{eq}_{PARPi-FL-PARP1}\right]\left[1 + \frac{\gamma}{\alpha}K \cdot \left(C_{PARP1} - C^{eq}_{PARPi-FL-PARP1}\right)\right] \quad (10)$$

The schematic principle of the brightness method is shown in Fig. 3.

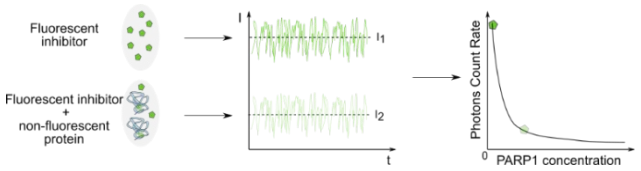

Fig. 3 Schematic of the brightness method. If only freely diffusing inhibitor molecules are present in the confocal volume, the fluorescence intensity (I_1) is higher than the fluorescence intensity of the sample after adding a certain concentration of PARP1 protein (CProtein ≫ Cinhibitor). Therefore, $I_1 > I_2$. By performing a series of measurements for a fixed concentration of inhibitor and an increasing concentration of the protein, a curve was obtained, from which the equilibrium constant of the protein – inhibitor reaction was determined.

Results and discussion

Olaparib analog penetration under 2D and 3D culture conditions

The study started by examining whether the fluorescent derivative of olaparib penetrates TNBC cells lacking BRCA1 mutation. For this purpose, we performed confocal imaging of MDA-MB-231 cells cultured under 2D conditions (Fig. 4E).

We observed that the higher signal recorded in the images came from the cytoplasm. Confocal imaging also revealed the presence of extracellular membrane-associated vesicles of MDA-MB-231 cells (Fig. S1A). These are likely to be oncosomes[14,15], taking diameters from 100 nm[16] to as much as 10 µm[17]. In our case, vesicles with a diameter of 2.25 µm predominated (Fig. S1B).

The study was expanded to include imaging under 3D culture conditions that better reflect the properties of cells in a tissue. Similar to 2D imaging, the inhibitor was present inside the cells. It was found that the fluorescent derivative of olaparib penetrates deep into the spheroid in less than 25 min which is in agreement with the results obtained *in vivo*[18]. Comparing Fig. 4G with Fig. 4H, it is hard to see the differences in the intensity of the recorded fluorescence signal depending on the incubation time of the spheroid with the drug, except for the larger background immediately after PARPi-FL addition. For a more detailed analysis, we compared the surface intensity plots at a depth of 25 µm of each spheroid since the measurement parameters for both scans were the same. Visible in Fig. S2 peaks in fluorescence intensity are deriving from intracellular PARPi-FL. The main difference that becomes evident in the progressive incubation time is the width of the individual peaks. After adding the PARPi-FL to the spheroid, the fluorescent analog of olaparib is at once present in the whole volume of cells. After 25 min, the fluorescence peaks are narrower. The change in breadth of fluorescence peaks implies that the tested inhibitor accumulates – probably on the nuclear membrane. Most importantly, in both cases (Fig. S2B,D), the maximum fluorescence intensity does not exceed 3000 AU – the penetration of olaparib in cells within spheroids is rapid and does not progress upon further incubation time. Using FCS, we verified that the compound was evenly distributed within subsequent layers of the spheroid after an incubation. For this purpose, concentrations in three consecutive layers of the spheroid were measured. The results, schematically shown in Fig. 4H, prove that the total drug concentration up to 30 µm into the spheroid is the same.

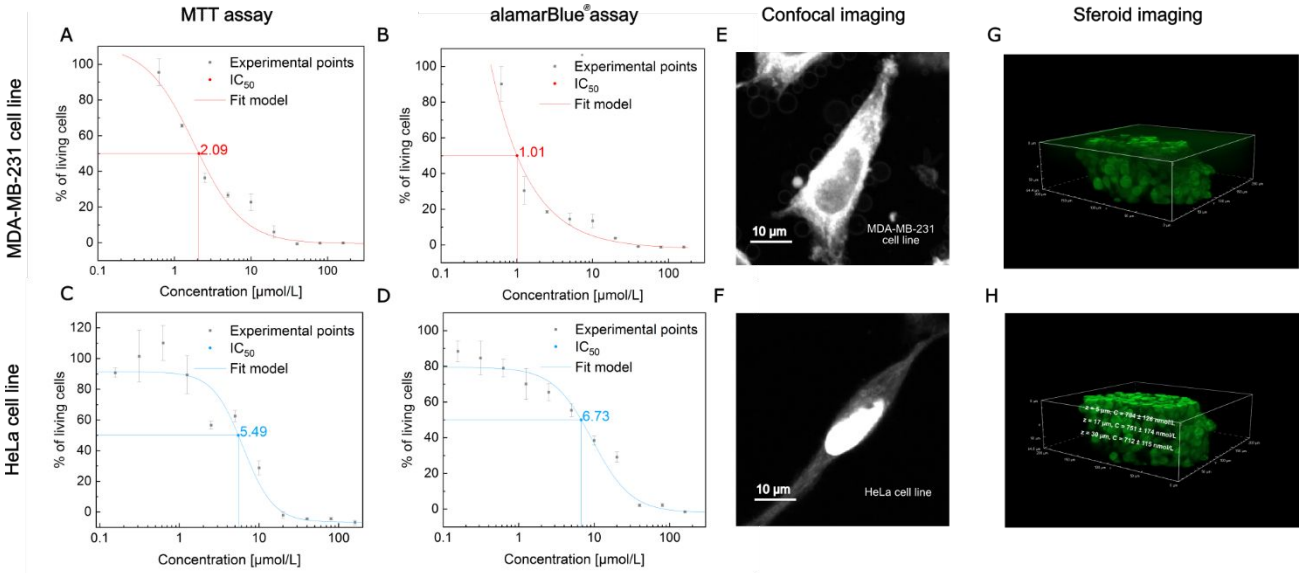

Fig. 4 Differences in olaparib analog cytotoxicity and distribution within the cell for CC and TNBC. (A, B) Viability of MDA-MB-231 cells incubated 72 hours with PARPi-FL as a function of compound concentration, with IC_{50} value based on MTT and alamarBlue® assay, respectively. (C, D) Viability of HeLa cells incubated 72 hours with PARPi-FL as a function of compound concentration, with IC_{50} value based on MTT and alamarBlue® assay, respectively. In all cases, a logistic dose-response function including four parameters, derived from the Origin2019b program, was fitted to the measurement points. Results indicate mean ± SD (n = 6) (E) Confocal imaging of MDA-MB-231 cells after incubation with PARPi-FL compound. (F) Confocal imaging of HeLa cells after incubation with PARPi-FL compound. (G) MDA-MB-231 spheroid imaged immediately (<2 min) after PARPi-FL addition. (H) MDA-MB-231 spheroid imaged after 25 min incubation. The green fluorescence signal was excited with a 485 nm laser and recorded with a spectral detector. PARPi-FL penetrates even into the deepest layers of the spheroid up to 70 µm from the glass. Picture H includes the results of PARPi-FL concentration measurements in three consecutive layers of MDA-MB-231 spheroid. The 3D structure of the spheroid was captured by acquiring images with a 0.12 µm step size. z = 0 corresponds to the first layer of the cells on the glass surface. For z = 5 µm the concentration of olaparib analog was C =784 ± 126 nmol/L, for z = 17 µm, C = 751 ± 174 nmol/L and for z = 30 µm, C = 712 ± 115 nmol/L.

To quantify the penetration effectiveness of the olaparib analog, we measured a partition coefficient[19] – the ratio of the intracellular drug concentration to extracellular drug concentration. The higher is the partition coefficient, the better effectiveness of uptake. The partition coefficient is a useful parameter in the determination of physiologically based pharmacokinetic (PBPK) models, and it can be applied to assess the distribution of a drug within a tissue. Moreover, in the case of a chemical that binds to a protein (like the tested olaparib), this parameter can be essential in the characterization of the saturable binding, which affects the distribution and elimination of a drug[19]. In the FCS approach, the partition coefficient can be easily determined by positioning the confocal focus inside and then outside cells and further analyzing the concentration from these two spots. The intracellular concentration was the sum of all concentrations of observed components in FCS. Detailed results for intracellular and extracellular concentrations for TNBC cultured under both 2D and 3D conditions are shown in Table S1.

We also examined Cervical Cancer (CC) cells (HeLa cell line) to verify if the penetration of the tested inhibitor is a cell type-specific property. HeLa cell line, similarly to MDA-MB-231 cells, does not have BRCA1 mutation. Confocal imaging (Fig. 4E,F) revealed a significant difference in the distribution of the tested compound between these two cell lines. We observed the accumulation of the olaparib analog in the nucleus in HeLa cells. Also, the extracellular vesicles seen in MDA-MB-231 cells were not visible in CC cells. Therefore, it can be assumed that oncosomes are property specific for a particular type of tumor cells. The presence of oncosomes can be associated with olaparib release[20], which significantly affects the drug concentration in cells. Moreover, the penetration effectiveness, measured as the partition coefficient, of PARPi-FL into CC cells was 1.5 times higher compared to TNBC. The partition coefficient values obtained under 2D and 3D culture conditions are presented graphically (Fig. 5D) to better visualize the differences between the tested cell lines. Under 3D culture conditions, both tested cell lines take up about two times more of the olaparib analog than in 2D. It is known that culture conditions have essential meaning for the morphology of cells, the organization of cytoskeleton filaments, or cell adhesion[21]. In 3D cell culture, cells adhere to the extracellular matrix, which is a porous scaffold enabling undisturbed drug access to the entire surface of the cell[10]. Moreover, a significant difference in PARP1 expression, and thus a number of drug targets, was observed between 2D and 3D cells[22]. The obtained results are summarized in Table 1.

Cytotoxicity of olaparib analog for TNBC and CC cells without BRCA1 mutation

We performed two independent cytotoxicity assays: MTT and alamarBlue®, to investigate whether drug accumulation in the nucleus (olaparib's site of action) of HeLa cells translates into a therapeutic effect. We used the MTT assay to determine the concentration of PARPi-FL causing inhibition of mitochondrial dehydrogenase activity, while alamarBlue® to find the concentration of metabolic reduction reaction of resazurin dye. For more details, please see Supplementary Information, SI4.

Both methods showed that concentrations of several µmol/L of the tested drug caused inhibition of growth of half of both tested types

of cells. For MDA-MB-231, the IC_{50} value determined by the alamarBlue® method was 1.01 µmol/L (Fig. 4B), which was about twice lower than from the MTT assay (2.09 µmol/L) (Fig. 4A). IC_{50} concentrations for HeLa cells were higher: 6.73 µmol/L (Fig. 4D) and 5.49 µmol/L (Fig. 4C) based on alamarBlue® and MTT assay, respectively. The results showed that CC cells are more resistant to the fluorescent derivative of olaparib compared to TNBC cells.

According to the manufacturer's information and based on *in vitro* assays, the IC_{50} of PARPi-FL is 12.2 nmol/L[23]. However, depending on which metabolic process is the basis of the study, a different value can be obtained, as confirmed by measurements for olaparib[24,25].

studies recently reported[26]. For HeLa, the survival of cells incubated with olaparib at a concentration of 10 µM for 72 hours was above 60% based on the MTS assay[27]. Considering the above, it can be concluded that the fluorescent derivative of olaparib in both TNBC and CC may be involved in unexplored processes and be more toxic to cells than olaparib. It is also possible that the equilibrium constant between olaparib, PARP1 protein, and DNA is lower than for the fluorescent derivative of olaparib.

Cellular nanoviscosity as a tool for the identification of the compounds

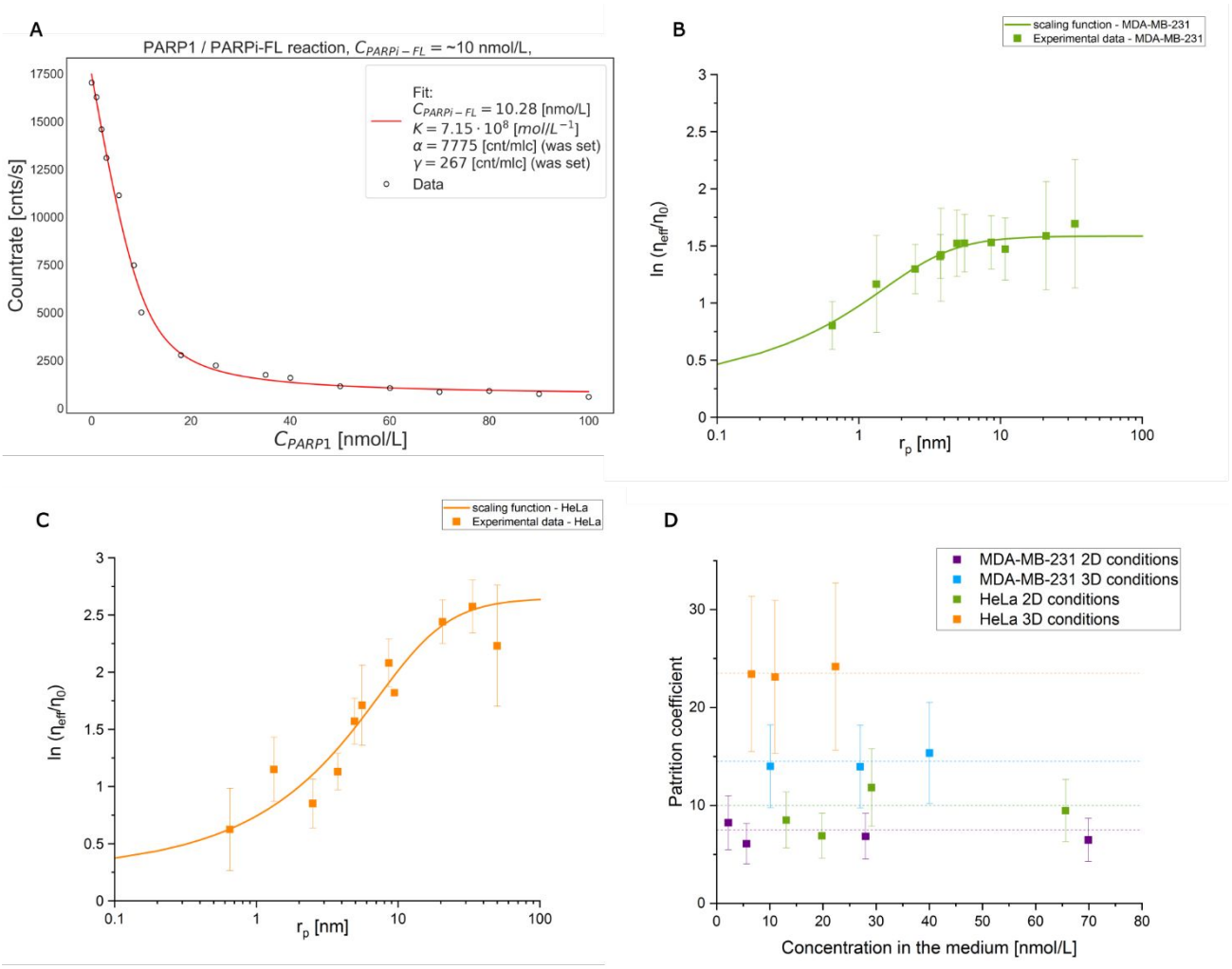

Fig. 5 Equilibrium constant of olaparib – PARP1 complex, cytoplasmic nanoviscosity and partition coefficient of HeLa and MDA-MB-231. (A) Equilibrium constant fit of PARP1 – olaparib analog complex from one of two independent experiments. The fit parameters were: concentration of PARPi-FL compound ($C_{PARPi-FL}$) and equilibrium constant (K). The molecular brightness of the freely diffusing PARPi-FL (α) and the PARP1 – olaparib analog complex (γ) were set. (B) Cytoplasm nanoviscosity curve obtained in the MDA-MB-231 cell line. (C) Cytoplasm nanoviscosity curve obtained in HeLa cell line[3]. For b and c, the scaling function (the mathematical model) is described by Equation 11, while the parameter values obtained after fitting are given in Table S3. (D) Dependence of partition coefficient on the concentration of olaparib analog in culture medium. Results are shown for both tested cell lines: MDA-MB-231 and HeLa, including 2D and 3D culture conditions. For graphs B and C, results indicate mean ± SD (number of tested cells N = 15), while for graph D, the error bars correspond to total differential method (number of tested cells N = 12).

From MTT assays on TNBC cells incubated with olaparib, an IC_{50} of 13.5 µmol/L was obtained[26], which is ten times higher than the results from the experiments performed for PARPi-FL. Presented studies also found that the fluorescent derivative showed efficacy for TNBC lacking BRCA1 mutation, which is in good agreement with

FCS measurements directly in living cells allow us to determine the interactions with PARP1 that a tested compound undergoes at a quantitative level. It has been shown that proper analysis of the mobility of the molecules in complex liquids requires considering the nanoviscosity of the probed system[28]. The nanoviscosity of the cell

nucleus was determined previously[4], while the cytoplasm nanoviscosity we defined by the dependence:

$$\eta_{eff} = \eta_0 \, A \, exp\left[\left(\frac{\xi^2}{R_H{}^2} + \frac{\xi^2}{r_p{}^2}\right)^{-a/2}\right] \quad (11)$$

Table 1 Comparison of quantitative data (concentrations and fractions of individual components in the nucleus, total concentration of PARP1 protein in the cytosol, concentration of free PARP1 protein in the nucleus, concentration of PARP1 protein bound to DNA, and partition coefficient determined under 2D and 3D culture conditions) between MDA-MB-231 and HeLa cells. Errors were calculated using total differential method (number of tested cells N = 10; each cell was measured three times).

Cell line	Fraction of the component			The concentration of the component [nmol/L]			The concentration of PARP1 – olaparib analog complex in the cytoplasm [nmol/L]	The concentration of freely diffusing PARP1 protein in the nucleus [nmol/L][a]	The concentration of PARP1 protein bound to DNA [nmol/L][b]	Partition coefficient	
	Freely diffusing PARPi-FL	PARP1 – olaparib analog complex	olaparib analog – PARP1 – RNA complex	Freely diffusing PARPi-FL	PARP1 – olaparib analog complex	olaparib analog – PARP1 – RNA complex				3D	2D
MDA-MB-231	0.24 ± 0.08	0.50 ± 0.05	0.26 ± 0.06	12.95 ± 3.89	28.04 ± 2.72	16.34 ± 2.86	67.96 ± 1.03	32.45 ± 5.98	219.77	14.33 ± 4.54	6.92 ± 2.34
HeLa	0.03 ± 0.02	0.67 ± 0.02	0.30 ± 0.01	15.19 ± 10.12	339.14 ± 9.11	151.85 ± 3.85	60.51 ± 0.95	355.85 ± 87.42	631.70	23.52 ± 0.45	9.06 ± 1.78

[a] based on the equilibrium constant in a buffer,[b] based on proteomic data[29].

where η_{eff} is the effective viscosity of cytoplasm, η_0 stands for the viscosity of water, A corresponds to a preexponential factor of the order of one, ξ and R_H are length scales characteristic for a cell line, a is an exponent smaller than 1 and r_p stands for the hydrodynamic radius of a tested probe. For more details, see work[3,5]. Based on the effective viscosity measurements, it is possible to determine the predicted diffusion coefficient inside the cell for a molecule of known hydrodynamic radius.

We quantified parameters a, ξ, and R_H for each of the examined cell lines separately (Table S3). The cytoplasmic nanoviscosity of MDA-MB-231 cells was determined for this study. The experimental data obtained with the mathematical model are shown in Fig. 5B.

The size of olaparib analog alone and in complex with PARP1 protein

After obtaining the nanoviscosity curves, we determined the sizes of the olaparib analog and the PARP1 protein – inhibitor complex in PBS solution. An example of structure size approximation is the hydrodynamic radius, which is a radius of an idealized sphere with a translational diffusion coefficient D (calculated according to Stokes-Sutherland-Einstein relation (3)) equal to the measured one. The hydrodynamic radii of the probes were calculated from the FCS measurements of diffusion coefficient, which are summarized in Table S4, and the exemplary autocorrelation curves are shown in Fig. S3. It is a good approximation in case of globular proteins, however less accurate in case of more complex shapes and may be a source of confusion when linking the molecular mass of the particle with its hydrodynamic properties.

PARP1 protein is made of six well-structured segments connected with flexible and approximately inextensible linkers[30], thus to relate the structure with measured diffusion coefficient more elaborate procedure is required. The diffusion coefficient can be calculated from the simulated particle trajectory and, like in the case of experimental data, related to the particle's hydrodynamic radius. A solitary sphere undergoing three dimensional Brownian motion with diffusion coefficient D has a mean square displacement between the initial position and position at time t

$$msd(t) = \langle |r(t) - r(0)|^2 \rangle = 2DtTrI = 6Dt \quad (12)$$

where TrI is a trace of a unit tensor. Another possibility is to use analytical results[31] for the lower bound on the diffusion coefficient. Here we use the Brownian dynamics approach with the generalized Rotne-Prager-Yamakawa approximation of hydrodynamic interactions[32,33]. In order to conveniently interpret simulation result we introduce a Brownian time scale $\tau_B = a^2/3D$, after which a sphere having a reference radius a (and diffusion coefficient D (3)) has a mean square displacement $msd(\tau_B) = 2a^2$. For example, two spheres of equal radii a (Fig. S4) that are connected with a flexible and inextensible linker (center to center length l = 4a) have msd ($3\tau_B$) = $3.89a^2$. Consequently, the diffusion coefficient of the two is (3.89/6) D ≈ 0.65D and the hydrodynamic radius is (6/3.89) a ≈ 1.54a.

The latter is neither 2a nor the radius of a sphere having twice the volume of a single component.

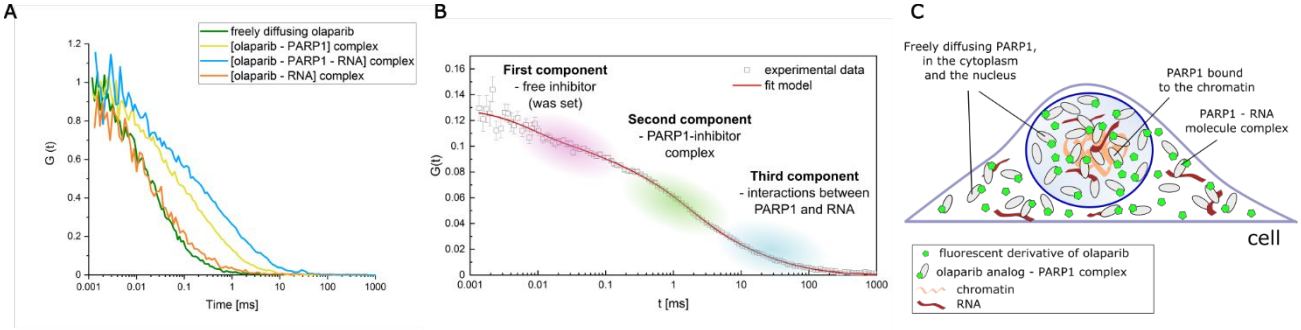

Fig. 6 Interpretation of FCS curves with a graphical scheme of its possible components. (A) Normalized FCS curves for the inhibitor alone, the olaparib analog – PARP1 protein complex, the olaparib analog – PARP1 protein – RNA complex, and the inhibitor – RNA mixture. From the shape of the curves, it can be seen that the fluorescent derivative of olaparib does not bind the RNA molecule. The diffusion coefficient is the same as for the inhibitor alone. (B) FCS autocorrelation curve from the MDA-MB-231 nucleus with the three-component diffusion model fitted. (C) Scheme of a cell showing the different fractions of the PARP1 protein: the freely diffusing cytoplasmic fraction, free PARP1 in the nucleus, the DNA-bound and RNA-bound protein. For more details, please see Table 1.

The PARP1 particle model consists of six beads and interconnecting linkers. Each bead represents a single structured segment with a hydrodynamic radius calculated based on its PDB structure. We used the GRPY package[34] for that purpose. It has recently been incorporated into the US-SOMO[35] software, which includes multiple bead model generators. The hydrodynamic radius of PARP1 calculated from its structure is approximately 6.9 nm that is 3.9 times larger than the hydrodynamic radius of its smallest constituent structure (3ODA in PDB), which we chose as reference radius (Fig. S4). The 5% discrepancy between measurement and first principle calculations provide additional confidence into experimental conduct. The modeling details are explained in the Supplementary Information, SI7.

Equilibrium constant of PARPi-FL and PARP1 protein in a buffer

Before the measurements in living cells, we determined the equilibrium constant of the PARP1 – olaparib analog complex by using the brightness method[12]. Measurements were performed for different concentrations of PARP1 protein, ranging from 1 nmol/L to 100 nmol/L, with a constant concentration of inhibitor. The dependence of the number of photons per second on the concentration of PARP1 protein is shown in Fig. 5A.

Upon inhibitor binding to the protein, the brightness of the fluorescent derivative of olaparib decreases, reflecting a drop in intensity with increasing PARP1 protein concentration. This results in an average equilibrium constant of $6.06 \cdot 10^8$ mol/L^{-1} (from two independent experiments), which agrees with the values of the dissociation constant of the PARP1 – olaparib complex[24]. At an inhibitor concentration of 10 nmol/L, the fluorescence intensity no longer changes significantly at a protein concentration of about 10 nmol/L, indicating one inhibitor molecule per protein molecule. The result reveals a high affinity of the drug for PARP1 protein.

Interactions of PARP1 protein with an RNA molecule

It is known that the PARP1 protein binds to DNA. Nonetheless, RNA has a similar chemical structure as DNA, which differs at the molecular level by only one nucleotide and carbohydrate core. RNA molecules are mobile and have different sizes, so that many of them could be a component of the FCS curve obtained in the cell. We performed an FCS experiment in a buffer to check whether the fluorescent complex PARPi-FL – PARP1 binds to RNA molecules (Supplementary Information, SI8).

We identified three components. The slowest component of the FCS curves (Fig. S6) was the olaparib analog – PARP1 – RNA complex. From the obtained diffusion coefficient, we calculated the hydrodynamic radius based on Equation 3, which was 57.10 ± 6.51 nm.

We performed a control experiment using the inhibitor with RNA molecule to exclude the possibility of their non-specific biding. The resulting diffusion coefficient was consistent with the diffusion coefficient of the free olaparib, indicating no interaction with RNA. Fig. 6A shows how to determine if an additional component is present in a sample based on the shape of the curve.

Quantitative analysis of cellular uptake of olaparib analog in the nucleus of TNBC and CC cells

Confocal imaging revealed that the fluorescent derivative of olaparib is present in the nucleus of MDA-MB-231 cells. We confirmed that by quantitative FCS measurements. The tested inhibitor binds to the freely diffusing PARP1 protein in 50.1 %, irrespectively of external concentration used in the study. For HeLa Kyoto, the presence of free PARP1 was reported previously[36]. The remaining percentage is represented by free PARPi-FL (23.8 %) and interactions of PARP1 protein with nuclear RNA. An example of an FCS curve with the fit model and components indication is shown in Fig. 6B. The PARP1 – olaparib analog complex was identified based on nucleus nanoviscosity by comparing the predicted diffusion coefficient[4] with the coefficient obtained in MDA-MB-231 cells (Table S7).

The third, slowest component of the FCS curve showed great diversity. The diffusion coefficient of this component took values ranging from 3.6 to 0.2 μm^2/s (Fig. S7). Based on the previously mentioned measurements in the buffer (Supplementary Information, SI8), we interpreted that the slowest component corresponds to interactions of the PARP1 – olaparib analog complex with RNA molecules present in the nucleus. From the obtained *in vitro* diffusion coefficient of the third component (Supplementary Information, SI8), its diffusion coefficient in the nucleus was estimated to be 0.99 μm^2/s using the nucleus nanoviscosity curve[4].

This value is similar to the average (0.8 $\mu m^2/s$) of the diffusion coefficient of the third component detected in the nucleus of TNBC cells. It proved that one of the components present in the nucleoplasm is likely to be a complex consisting of an RNA molecule, the PARP1 protein, and the tested inhibitor. Moreover, the ability of PARP proteins to bind to RNA molecules has been demonstrated previously[37].

The large range of the third component diffusion coefficient may be due to the interactions that RNA undergoes in the cell nucleus, such as interaction with chromatin[38] and proteins[39]. In addition, nuclear RNA is known to exhibit a large distribution, from a half-length in the range of 10-15 kb to very short molecules[40]. For example, the diffusion coefficient of different types of RNA molecules in mammalian cells can vary from 0.04 to 1.9 $\mu m^2/s$[41].

We also conducted the quantitative FCS measurements for PARPi-FL uptaken by HeLa cell line, in which the drug was accumulated in the nucleus, as shown on the confocal images. A significant difference at the quantitative level between TNBC and CC was observed. The PARPi-FL concentration inside the nucleus of HeLa cells was around ten times higher than the one observed in the nucleus of MDA-MB-231 cells at the same external drug concentration. Moreover, we noted crucial differences in the fractions of the individual components. For HeLa cells, the amount of freely diffusing drug was almost tenfold lower (about 3% of the total concentration of the compound), compared to the fastest fraction inside MDA-MB-231 cells. Based on the concentrations of the freely diffusing inhibitor as well as the PARP1 – olaparib analog complex and the equilibrium constant determined in PBS solution, we defined the amount of PARP1 protein freely diffusing in the nucleus of both cell types. These values were 32.45 nmol/L for MDA-MB-231 and 355.85 nmol/L for HeLa, respectively. Thus, a more than the tenfold higher abundance of PARP1 unbound to the genetic material was noted for CC. The equilibrium constant *in vivo* was assumed to be the same as *in vitro* due to the lack of significant nanoviscosity changes between cells and buffer for probes with hydrodynamic radii less than 10 nm[5].

Moreover, we determined the total PARP1 protein concentrations for both cancer types, based on the proteomic data[29] and knowing the cell volumes (6 900 μm^3 for HeLa cells and 8 400 μm^3 for MDA-MB-231, determined using NIS-Elements software). After subtracting the concentrations of PARP1 protein bound to RNA, present in the cytoplasm and freely diffusing in the nucleus, we obtained the concentrations of DNA-bound PARP1. This concentration was equal to 631.70 nmol/L for HeLa cells, while for TNBC cells – 219.77 nmol/L. This higher DNA-bound PARP1 abundance in CC may be due to both the greater accumulation of DNA damage in these cells and the greater importance of the PARP protein-mediated repair pathway of the resulting breaks in genetic material.

Based on the performed quantitative FCS analysis, we found that observed differences in the distribution of olaparib derivative between HeLa and MDA-MB-231 cells rely on the expression levels of PARP1 protein of both cell lines. PARP1 protein expression level in CC is significantly higher than in TNBC (Western blot assay)[27]. This is also confirmed by proteomic data[29] (337 nmol/L for MDA-MB-231 and 1200 nmol/L for HeLa after considering the cell volume). Thus, more PARP1 protein in HeLa cells indicates an increase in the amount of protein-associated probe (the second component in our FCS measurements). A summary of the observed differences between cells as the quantitative results is shown in Table 1.

According to the presented results, it can be said that higher resistance to the tested olaparib analog is positively correlated with PARP1 protein expression. From the literature, it is known that the overexpression of PARP1 protein in breast cancer stem cells is associated with resistance to olaparib[42]. Moreover, for neuroblastoma cases[43] and breast cancer[44], high levels of PARP1 expression are associated with a poor prognosis. However, it is also important to note that the tested cell lines are free of BRCA1 mutation. The BRCA1 protein is involved in the repair of olaparib-induced DNA damage. So the more BRCA1 protein there is, the more effective the repair processes are. Based on the literature, it is known that HeLa cells produce significantly more BRCA1 protein compared to TNBC cells[27]. Moreover, from proteomic data[29], it is known that the HeLa cell line is the second most-producing BRCA1 protein. All of this leads to the conclusion that despite the higher accumulation of the drug in tissues (HeLa), the therapeutic effect is closely related to the amount of BRCA1 protein. Thus, it is clear that the best treatment effects with PARP inhibitors will be found in TNBC patients without the BRCA1 mutation. However, even cells having BRCA1 protein but in low amounts are sensitive to olaparib.

PARP1 protein present in the cytoplasm of TNBC and CC cells

We performed analogous studies for the cytoplasm of MDA-MB-231 and HeLa cells. The obtained FCS autocorrelation curves were fitted with the same model as in the nucleus. Similarly, component identification was performed based on the scale-dependent cytoplasm viscosity model (Equation 11, Table S3). Based on FCS curves analysis, the second component in the cytoplasm of TNBC was found to correspond, as in the nucleus, to the PARP1 – olaparib analog complex. A comparison of the predicted diffusion coefficient of PARP1 protein in the cytoplasm with the obtained diffusion coefficient is shown in Table S7.

The third component present in the cytoplasm of MDA-MB-231 took similar values as in the nucleus with the average equal to 0.83 ± 0.29 $\mu m^2/s$, which stands for a hydrodynamic radius of 78 nm. It corresponds to non-specific binding, probably to cytoplasmic mRNA [45]. In accordance with the previously mentioned measurements of RNA with PARP1 in a buffer (Supplementary Information, SI8), it is known that the size of the 2,000 nt RNA molecule is 57.10 ± 6.51 nm. Based on the cytoplasmic nanoviscosity of MDA-MB-231 cells (Fig. 5B), a diffusion coefficient of 1.14 ± 0.30 $\mu m^2/s$ was calculated. This value is within the error of the coefficient obtained from the cytosol.

For HeLa, identification of the components revealed that the second component of the CC cytoplasm corresponds, as in the cytoplasm of MDA-MB-231, to the PARP1 – olaparib analog complex. The predicted and obtained diffusion coefficient was respectively 7.45 ± 0.43 $\mu m^2/s$ and 6.48 ± 1.23 $\mu m^2/s$. The diffusion coefficient of the third slowest component of the cytoplasm was 0.58 ± 0.61 $\mu m^2/s$. Based on the cytoplasm nanoviscosity of HeLa (Fig. 5C), most likely, this component is also responsible for interactions with cytoplasmic mRNA.

Expression of PARP1 protein in the cytoplasm of breast cancer was reported previously[46,47]. Moreover, it was shown that the high expression of cytoplasmic PARP in TNBC correlates with an aggressive tumor course and predicting an unbeneficial long-term prognosis. As described previously, the presence of cytoplasmic PARP1 may become a predictive marker for the activity of PARP inhibitors[48]. However, this study showed that the inhibitor – protein complex concentration in the cytoplasm for both tested cell lines was virtually the same while the therapeutic effect differed. Thus, the statement about the predictive potential of the cytoplasmic form of the PARP1 protein seems doubtful.

Conclusions

In this study, for the first time, we presented quantitative data on the penetration of olaparib analog into TNBC cells (MDA-MB-231 cell line), comparing them with results for CC cells. We pinpointed which components (freely diffusing inhibitor, PARP1 – olaparib analog complex, and olaparib analog – PARP1 – RNA complex) and at what concentrations are present in the cell nucleus after incubation with the fluorescent derivative of olaparib, PARPi-FL. PARP1 protein was identified not only in the nucleus of cancer cells but also in the cytoplasm of both tested cell lines. In the case of HeLa cells, the presence of cytoplasmic PARP1 was reported for the first time. However, we proved that PARP1 protein levels in the cytoplasm are not associated with the therapeutic effect. For both cell lines, the concentrations of this component were very similar (60.51 nM for HeLa and 67.96 nM for MDA-MB-231), while the resistance of HeLa cells was higher.

We noted numerous differences between TNBC cells and CC cells. HeLa cell line was more resistant to the fluorescent derivative of olaparib. Confocal imaging showed the accumulation of the tested inhibitor in the nucleus of CC cells. Moreover, the effectiveness of penetration of the tested inhibitor into HeLa cells based on the partition coefficient determined under 2D and 3D culture conditions was about 1.5 times higher. In contrast, MDA-MB-231 showed oncosomes, vesicles characteristic of tumor cells, which presence does not appear to be relevant to the success of PARP inhibitor therapy. Our novel approach of quantitative FCS analysis directly in living cells proved what was seen on imaging. In the HeLa nucleus, the total concentration of olaparib analog was approximately 10-fold higher. Based on the literature and proteomic data, we know that drug accumulation in the nucleus is related to the amount of PARP1 protein, just as the effectiveness of penetration depends on the abundance of the drug target, which in the case of olaparib is PARP1 protein. Thus, olaparib is an example of a targeted therapy that acts on cells with specific determinants. Importantly, the effectiveness of drug penetration and accumulation at the site of action, which is the cell nucleus, does not imply the success of the therapy. Both cell lines tested are lacking BRCA1 mutation. The FDA approves the use of a PARP inhibitor drug for patients diagnosed with TNBC carrying BRCA1 mutation because only then the DNA damage caused by olaparib is not repaired. However, the results presented in this study are evidence that also cell lines without BRCA1 mutations can be sensitive to the used inhibitor, like MDA-MB-231. Sensitivity understood as the success of therapy is closely correlated with the amount of BRCA1 protein. HeLa cells produce significantly more of this protein, making them more resistant to the tested inhibitor.

Data availability

All data needed to evaluate the conclusions are present in the paper and in the associated supplementary material.

Author Contributions

The concept and scheme of the study were created by A.K, G.M, K.Kwapiszewska and R.H. The experiments were performed by A.K, M.P, and J.B. K. Kucharska assisted with brightness method measurements. P.Ż. conducted the GRPY modeling. Data analysis and result discussion were performed by A.K, K.Kwapiszewska, M.P, J.B, G.M, K. Kucharska and R.H. A.K, K.Kwapiszewska, M.P, K. Kucharska, J.B, P.Ż, G.M, and R.H. drafted the article.

Conflicts of interest

There are no conflicts to declare.

Acknowledgements

The authors want to thank Krzysztof Bielec for the Python manuscript allowing analysis of the data obtained with the Brightness Method. This research was funded by the National Centre for Research and Development, Poland, grant number [LIDER/10/0033/L-9/17/NCBR/2018].

Notes and references

1 K. Okamoto and Y. Sako, *Curr. Opin. Struct. Biol.*, 2017, **46**, 16–23.
2 A. Xiwei, Z. Cong, B. Zhao, L. Maria and P. David, *J. Pharm. Biomed. Anal.*, 2015, **113**, 163–180.
3 K. Kwapiszewska, T. Kalwarczyk, B. Michalska, K. Szczepański, J. Szymański, P. Patalas-Krawczyk, T. Andryszewski, M. Iwan, J. Duszyński and R. Hołyst, *Sci. Rep.*, 2019, **9**, 1–9.
4 G. Bubak, K. Kwapiszewska, T. Kalwarczyk, K. Bielec, T. Andryszewski, M. Iwan, S. Bubak and R. Hołyst, *J. Phys. Chem. Lett.*, 2021, **12**, 294–301.
5 K. Kwapiszewska, T. Kalwarczyk, B. Michalska, K. Kwapiszewska, K. Szczepan, T. Andryszewski, M. Iwan, J. Duszyn, P. Patalas-krawczyk and R. Ho, *J. Phys. Chem. Lett.*, 2020, **11**, 6914–6920.
6 E. C. Friedberg, D. H. Castrillon, R. L. Galindo and K. A. Wharton, *New-opathies: An emerging molecular reclassification of human disease*, 2012.
7 J. M. Pascal, *DNA Repair (Amst).*, 2018, **71**, 177–182.
8 S. Tangutoori, P. Baldwin and S. Sridhar, *Maturitas*, 2015, **81**, 5–9.
9 L. Nagy, B. Rauch, N. Balla, G. Ujlaki, G. Kis, O. Abdul-rahman, E. Kristóf, A. Sipos, M. Antal, A. Tóth, T. Debreceni and A. Horváth, *Biochem. Pharmacol.*, 2019, **167**, 76–85.
10 M. Pilz, K. Kwapiszewska, T. Kalwarczyk, G. Bubak, D. Nowis and R. Hołyst, *Nanoscale*, 2020, **12**, 19880–19887.
11 T. Kalwarczyk, K. Kwapiszewska, K. Szczepanski, K. Sozanski, J. Szymanski, B. Michalska, P. Patalas-Krawczyk, J. Duszynski and R. Holyst, *J. Phys. Chem. B*, 2017, **121**, 9831–9837.
12 Y. Zhou, K. Bielec, P. Pasitsuparoad and R. Hołyst, *Analyst*, 2020, **145**, 6600–6606.
13 K. Bielec, G. Bubak, T. Kalwarczyk and R. Holyst, *J. Phys. Chem. B*, 2020, **124**, 1941–1948.
14 P. K. Wright, S. B. Jones, N. Ardern, R. Ward, B. Clarke, F. Sotgia, M. P. Lisanti, G. Landberg and R. Lamb, *Oncotarget*, 2014, **5**, 3055–3065.
15 D. Di Vizio, M. Morello, A. C. Dudley, P. W. Schow, R. M. Adam, S. Morley, D. Mulholland, M. Rotinen, M. H. Hager, L. Insabato, M. A. Moses, F. Demichelis, M. P. Lisanti, H. Wu, M. Klagsbrun, N. A. Bhowmick, M. A. Rubin, C. D. Souza-schorey and M. R. Freeman, *Am. J. Pathol.*, 2012, **181**, 1573–1584.
16 K. Al-Nedawi, B. Meehan, J. Micallef, V. Lhotak, L. May, A.

Guha and J. Rak, *Nat. Cell Biol.*, 2008, **10**, 619–624.
17 V. R. Minciacchi, S. You, C. Spinelli, S. Morley, M. Zandian, P. Aspuria, L. Cavallini, C. Ciardiello, M. R. Sobreiro, M. Morello, G. Kharmate, S. C. Jang, D. Kim, E. Hosseini-beheshti, E. T. Guns, Y. S. Gho, S. Mathivanan, W. Yang and M. R. Freeman, *Oncotarget*, 2015, **6**, 11327–11341.
18 B. Carney, S. Kossatz and T. Reiner, *J. Nucl. Med.*, 2017, **58**, 1025–1030.
19 G. Johanson, in *Comprehensive Toxicology: Second Edition*, 2010, vol. 1–14, pp. 153–177.
20 T. Eguchi, E. A. Taha, S. K. Calderwood and K. Ono, *Biology (Basel).*, 2020, **9**, 1–22.
21 C. P. Soares, V. Midlej, M. E. W. de Oliveira, M. Benchimol, M. L. Costa and C. Mermelstein, *PLoS One*, 2012, **7**, e38147.
22 S. Kopp, J. Sahana, T. Islam, A. G. Petersen, J. Bauer, T. J. Corydon, H. Schulz, K. Saar, N. Huebner, L. Slumstrup, S. Riwaldt, M. Wehland, M. Infanger and R. Luetzenberg, *Sci. Rep.*, 2018, **8**, 1–17.
23 B. Carney, S. Kossatz, B. H. Lok, V. Schneeberger, K. K. Gangangari, N. V. K. Pillarsetty, W. A. Weber, C. M. Rudin, J. T. Poirier and T. Reiner, *Nat. Commun.*, 2018, **9**, 1–13.
24 T. A. Hopkins, Y. Shi, L. E. Rodriguez, L. R. Solomon, C. K. Donawho, E. L. Di Giammarino, S. C. Panchal, J. L. Wilsbacher, W. Gao, A. M. Olson, D. F. Stolarik, D. J. Osterling, E. F. Johnson and D. Maag, *Mol. Cancer Res.*, 2015, **13**, 1465–1477.
25 H. Zhao, Q. Yang, Y. Hu and J. Zhang, *Oncol. Rep.*, 2018, **40**, 3223–3234.
26 M. Y. Keung, Y. Wu, F. Badar and J. V. Vadgama, *J. Clin. Med.*, 2020, **9**, 940.
27 E. Kukolj, T. Kaufmann, A. E. Dick, R. Zeillinger, D. W. Gerlich and D. Slade, *Oncotarget*, 2017, **8**, 103931–103951.
28 T. Kalwarczyk, N. Ziębacz, A. Bielejewska, E. Zabokoklicka, K. Kyonov, J. Szymański and W. Agnieszka, *Nano Lett.*, 2011, **11**, 2157–2163.
29 ProteomicDB powered by SAP HANA.
30 J. D. Steffen, M. M. McCauley and J. M. Pascal, *Nucleic Acids Res.*, 2016, **44**, 9771–9783.
31 B. Cichocki, M. Rubin, A. Niedzwiecka and P. Szymczak, *J. Fluid Mech.*, 2019, **878**, 1–12.
32 E. Wajnryb, K. A. Mizerski, P. J. Zuk and P. Szymczak, *J. Fluid Mech.*, DOI:10.1017/jfm.2013.402.
33 B. Cichocki, P. Szymczak and P. J. Żuk, *J. Chem. Phys.*, DOI:10.1063/5.0030175.
34 P. J. Zuk, B. Cichocki and P. Szymczak, *Biophys. J.*, 2018, **115**, 782–800.
35 E. Brookes and M. Rocco, *Eur. Biophys. J.*, 2018, **47**, 855–864.
36 M. Kozłowski, PhD thesis, der Ludwig – Maximilians – Universität München, 2014.
37 M. Y. Nakamoto, J. Rudolph, D. S. Wuttke and K. Luger, *Biochemistry*, 2019, **58**, 5107–5111.
38 W. Wu, Z. Yan, T. C. Nguyen, Z. Bouman Chen, S. Chien and S. Zhong, *Nat. Protoc.*, 2019, **14**, 3243–3272.
39 A. Balcerak, A. Trebinska-Stryjewska, R. Konopinski, M. Wakula and E. A. Grzybowska, *Open Biol.*, DOI:10.1098/rsob.190096.
40 M. Di Giulio and M. Kreitman, *J. Mol. Evol.*, 1980, **15**, 35–57.
41 C. Molenaar, A. Abdulle, A. Gena, H. J. Tanke and R. W. Dirks, *J. Cell Biol.*, 2004, **165**, 191–202.
42 M. Gilabert, S. Launay, C. Ginestier, F. Bertucci, S. Audebert, M. Pophillat, Y. Toiron, E. Baudelet, P. Finetti, T. Noguchi, H. Sobol, D. Birnbaum, J. P. Borg, E. Charafe-Jauffret and A. Gonçalves, *PLoS One*, 2014, **9**, 6–11.
43 V. Colicchia, M. Petroni, G. Guarguaglini, F. Sardina, M. Sahún-Roncero, M. Carbonari, B. Ricci, C. Heil, C. Capalbo, F. Belardinilli, A. Coppa, G. Peruzzi, I. Screpanti, P. Lavia, A. Gulino and G. Giannini, *Oncogene*, 2017, **36**, 4682–4691.
44 F. Rojo, J. García-Parra, S. Zazo, I. Tusquets, J. Ferrer-Lozano, S. Menendez, P. Eroles, C. Chamizo, S. Servitja, N. Ramírez-Merino, F. Lobo, B. Bellosillo, J. M. Corominas, J. Yelamos, S. Serrano, A. Lluch, A. Rovira and J. Albanell, *Ann. Oncol.*, 2012, **23**, 1156–1164.
45 Z. B. Katz, B. P. English, T. Lionnet, Y. J. Yoon, N. Monnier, B. Ovryn, M. Bathe and R. H. Singer, *Elife*, 2016, **5**, 1–16.
46 P. Domagala, T. Huzarski, J. Lubinski, K. Gugala and W. Domagala, *Breast Cancer Res. Treat.*, 2011, **127**, 861–869.
47 P. Donizy, G. Pietrzyk, A. Halon, C. Kozyra, T. Gansukh, H. Lage, P. Surowiak and R. Matkowski, *Oncol. Rep.*, 2014, **31**, 1777–1787.
48 G. Von Minckwitz, B. M. Müller, S. Loibl, J. Budczies, C. Hanusch, S. Darb-Esfahani, J. Hilfrich, E. Weiss, J. Huober, J. U. Blohmer, A. Du Bois, D. M. Zahm, F. Khandan, G. Hoffmann, B. Gerber, H. Eidtmann, F. Fend, M. Dietel, K. Mehta and C. Denkert, *J. Clin. Oncol.*, 2011, **29**, 2150–2157.